Latin American Journal of Solids and Structures
www.lajss.org

Local buckling in tridimensional frames: experimentation and simplified analysis

Abstract

Bidirectional-loading tests are carried out to examine the behavior of thin-walled circular and rectangular steel elements and a tridimensional framed structure. The experimental results were used to confirm the validity of the lumped damage mechanical approach to model the post-local buckling structural behavior. In this approach, local buckling is lumped at plastic hinges. The degree of local buckling is represented by a vectorial damage variable. The implementation of the model in a finite element program is also described.

Keywords

Steel Hollow Elements; Tridimensional Steel Structures; Nonlinear Analysis; Local Buckling; Lumped Damage Mechanics.

María E. Marante[a], Ricardo Picón[a], Néstor Guerrero[a] and Julio Flórez-López[a,b]

aLaboratory of Structural Mechanics, Lisandro Alvarado University,
Av. La Salle, Barquisimeto 3001, Venezuela
bStructural Engineering Department, University of Los Andes,
Sector La Hechicera, Mérida 5101, Venezuela

1 INTRODUCTION

Design codes incorporate new concepts related to limit values of damage and residual deformations in steel structures. Thus, comprehensive experimental studies as well as efficient and accurate models for this kind of structures are important; specifically for the post local-buckling phase.

So far, most experimental analyses are limited to the case of unidirectional loading, however real cases involve complex and multidirectional actions. Only a limited number of studies deal with general bidirectional loading; amongst them Watanabe *et al.* [1], Goto *et al.* [2] and Guerrero *et al.* [3]. In those papers, rectangular and circular columns were subjected to complex two-dimensional loading paths. In Goto *et al.* [2] it is indicated that the coupling of the two horizontal components has an unfavorable effect on the ultimate behavior of columns.

The number of studies on steel framed structures is also limited; most of them deal only with planar frames (Fahnestock *et al.* [4], Qu *et al.* [5], Annan *et al.* [6]) or trusses (Wood and Dawe [7]). Nakashima *et al.* [8] report a test on a tridimensional steel structure with reinforced concrete floor slab, however only unidirectional loading was considered.

The numerical analysis of local-buckling can be carried out using nonlinear shell theory (see for instance, Goto *et al.* [2], Salem *et al.* [9], Nowzartash and Mohareb [10]). However, this approach is limited to the case of parts of the structure and not to the entire tridimensional frame. A second possibility is the use of fiber or beam theories (Bebiano *et al.* [11], Degee *et al.*[12]). Although this is a more accessible approach, the analysis of complex tridimensional frames is still out of its reach. A convenient approach that combines simplicity with a good enough description for engineering purposes is lumped damage mechanics (Inglessis *et al.* [13], Febres *et al.* [14]). However, in those papers the model was limited to planar frames. Guerrero *et al.* [3] generalized the model to the case of hollow steel elements subjected to bidirectional loading.

The present paper reports an experimental study on thin-walled elements as well as a tridimensional steel frame with reinforced concrete floor slab subjected to complex bidirectional loadings. These tests were simulated using the aforementioned biaxial model in order to appreciate the advantages and limitations of the lumped damage mechanics approach.

2 NUMERICAL ANALYSIS OF LOCAL BUCKLING

2.1 Kinematics and statics of 3D frames

Consider a tridimensional frame with m elements connected by n nodes as shown in Fig. 1. A set of global orthogonal coordinate axis X, Y and Z is introduced in order to describe the movement of the structure in the time interval [0,T]. The matrix of generalized displacements, or degrees of freedom, of a node i of the frame is given by $\mathbf{u}_i^t = (u_i, v_i, w_i, \theta_i, \vartheta_i, \phi_i)$, where t means "transpose", $\mathrm{u_i}$, $\mathrm{v_i}$ and $\mathrm{w_i}$ represent displacements in, respectively, the X, Y and Z directions while θ_i, ϑ_i, ϕ_i are the rotations around the same axes. The matrix of generalized displacements of the frame is given by $\mathbf{U}^{\mathbf{t}} = (\mathbf{u}_1, \mathbf{u}_2, ..., \mathbf{u}_n)$. The matrix of external forces conjugated to the generalized displacement is denoted by F.

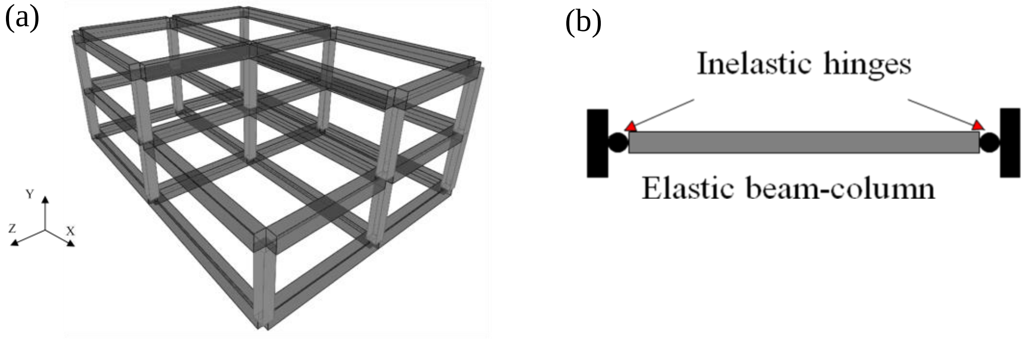

Fig. 1. (a) Tridimensional framed structure. (b) Lumped plasticity model

Consider an element e of the frame between nodes i and j. A system of local orthogonal coordinates axis x, y and z is introduced as shown in Fig. 2b. The generalized stress matrix is given by $\boldsymbol{\sigma}_{\mathrm{e}}^{\mathrm{t}} = (m_{iy}, m_{iz}, n, m_{jy}, m_{jz}, m_x)$ and the generalized strain matrix of the element is given by

$\boldsymbol{\varepsilon}_e^t = (\varphi_{iy}, \varphi_{iz}, \delta, \varphi_{jy}, \varphi_{jz}, \varphi_x)$ where the meaning of the symbols in the $\boldsymbol{\sigma}$ and $\boldsymbol{\varepsilon}$ matrices are shown, respectively in Figs. 2a and 2b.

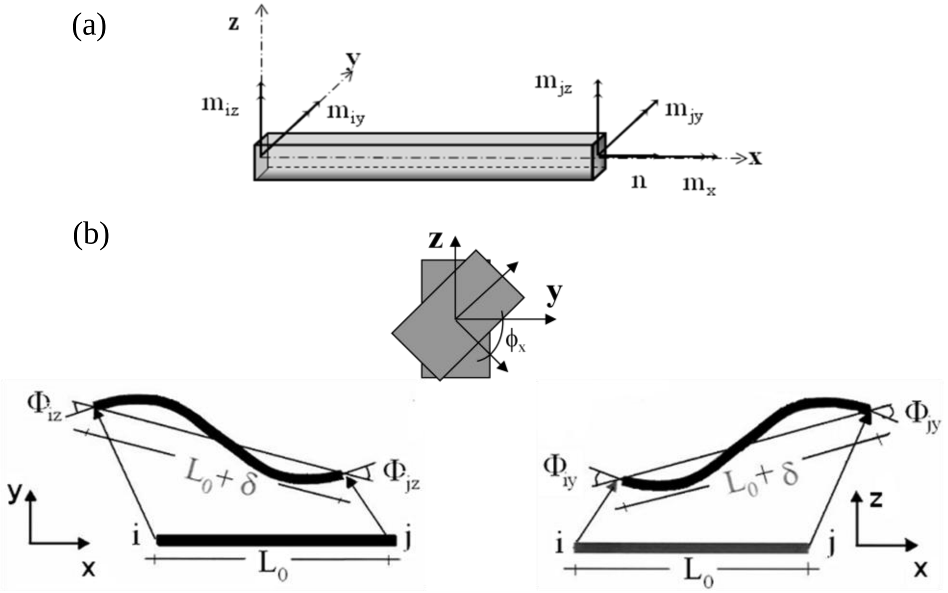

Fig. 2. (a) Generalized deformations of the frame member. (b) Generalized stresses of the frame member

The terms generalized stress and deformations are used as an extension of the conventional concepts of Cauchy stress tensor and strain tensor since the former variables have the same role of the later in the constitutive law of a frame element (see next section).

Notice that shear forces should not be included as independent variables in the generalized stress matrix since they are determined from the flexural moments via equilibrium equations of the frame element; for instance in the case of nil distributed forces on the element, the shear forces are $V_{iy} = V_{jy} = \dfrac{m_{iz} + m_{jz}}{L}$ and $V_{iz} = V_{jz} = \dfrac{m_{iy} + m_{jy}}{L}$, where L is the element length.

A relationship between generalized strains and generalized displacements can be obtained from geometrical considerations as:

$$\dot{\boldsymbol{\varepsilon}}_e = \mathbf{B}(\mathrm{U})_{\mathrm{e}}\dot{\mathrm{U}} \tag{1}$$

Where $\mathrm{B}(\mathrm{U})_{\mathrm{e}}$ is called transformation matrix of the element e. The dot over a variable means time derivative. The transformation matrix is given by:

$$\mathbf{B}(U)_e = \begin{bmatrix} -\frac{m_1}{L} & -\frac{m_2}{L} & -\frac{m_3}{L} & n_1 & n_2 & n_3 & \frac{m_1}{L} & \frac{m_2}{L} & \frac{m_3}{L} & 0 & 0 & 0 \\ -\frac{m_1}{L} & -\frac{m_2}{L} & -\frac{m_3}{L} & 0 & 0 & 0 & \frac{m_1}{L} & \frac{m_2}{L} & \frac{m_3}{L} & n_1 & n_2 & n_3 \\ -t_1 & -t_2 & -t_3 & 0 & 0 & 0 & t_1 & t_2 & t_3 & 0 & 0 & 0 \\ \frac{n_1}{L} & \frac{n_2}{L} & \frac{n_3}{L} & m_1 & m_2 & m_3 & -\frac{n_1}{L} & -\frac{n_2}{L} & -\frac{n_3}{L} & 0 & 0 & 0 \\ \frac{n_1}{L} & \frac{n_2}{L} & \frac{n_3}{L} & 0 & 0 & 0 & -\frac{n_1}{L} & -\frac{n_2}{L} & -\frac{n_3}{L} & m_1 & m_2 & m_3 \\ 0 & 0 & 0 & -t_1 & -t_2 & -t_3 & 0 & 0 & 0 & t_1 & t_2 & t_3 \end{bmatrix} \quad (2)$$

where m_i, n_i and t_i are the components of unit vectors in the x, y, and z directions with respect to the global system of reference. The principle of virtual power states that:

$$\sum_{e=1}^{m} (\dot{\boldsymbol{\varepsilon}}_e^*)^t \boldsymbol{\sigma}_e = (\dot{\mathbf{U}}^*)^t \mathbf{F} \quad (3)$$

where stars represent virtual quantities.

Substituting the kinematic equation (1) into Eq. (3) and taking into account that this relationship is valid for any virtual displacement; the following static equilibrium equation is obtained

$$\sum_{e=1}^{m} (\mathbf{B}(U)_e)^t \boldsymbol{\sigma}_e = \mathbf{F} \quad (4)$$

2.2 A simplified model of local buckling

Constitutive law for a frame element that includes local bucking has been proposed in [3]. The model is based on the lumped plasticity assumption; thus an element between nodes i and j is considered as the assemblage of an elastic beam-column and two inelastic hinges as it is shown in Fig. 1. Two sets of internal variables are now introduced. The first one is the generalized plastic strain $(\boldsymbol{\varepsilon}_e^p)^t = (\varphi_{iy}^p, \varphi_{iz}^p, \delta^p, \varphi_{jy}^p, \varphi_{jz}^p, \varphi_x^p)$, where φ_{iy}^p is the rotation of the plastic hinge i in the plane x-z, φ_{iz}^p is the rotation of the plastic hinge i in the plane x-y, δ^p is the permanent elongation of the element and φ_x^p is the torsional rotation of the element. Local bucking is assumed to be lumped at the plastic hinges as well. Therefore a local bucking damage variable is introduced: $(\mathbf{d}_e)^t = (d_{iy}, d_{iz}, d_{jy}, d_{jz})$. The meaning of the components is shown in Fig. 3. Damage parameters can take values between zero and one, where zero represents the absence of local bucking. The state law is given by:

$$\boldsymbol{\sigma}_e = \mathbf{S}_e(\mathbf{d}_e)(\boldsymbol{\varepsilon}_e - \boldsymbol{\varepsilon}_e^p) \quad (5)$$

where S_e is the stiffness matrix of the element e and it is given by:

$$\mathbf{S}_e\,(\mathbf{d}_e) = \begin{bmatrix} \dfrac{3S_{11}^0(1-d_{iy})}{4-(1-d_{iy})(1-d_{jy})} & \dfrac{3S_{12}^0(1-d_{iy})(1-d_{jy})}{4-(1-d_{iy})(1-d_{jy})} & 0 & 0 & 0 & 0 \\ \dfrac{3S_{21}^0(1-d_{iy})(1-d_{jy})}{4-(1-d_{iy})(1-d_{jy})} & \dfrac{3S_{22}^0(1-d_{jy})}{4-(1-d_{iy})(1-d_{jy})} & 0 & 0 & 0 & 0 \\ 0 & 0 & S_{33}^0 & 0 & 0 & 0 \\ 0 & 0 & 0 & \dfrac{3S_{44}^0(1-d_{iz})}{4-(1-d_{iz})(1-d_{jz})} & \dfrac{3S_{45}^0(1-d_{iz})(1-d_{jz})}{4-(1-d_{iz})(1-d_{jz})} & 0 \\ 0 & 0 & 0 & \dfrac{3S_{54}^0(1-d_{iz})(1-d_{jz})}{4-(1-d_{iz})(1-d_{jz})} & \dfrac{3S_{55}^0(1-d_{jz})}{4-(1-d_{iz})(1-d_{jz})} & 0 \\ 0 & 0 & 0 & 0 & 0 & S_{66}^0 \end{bmatrix} \qquad (6)$$

The terms S_{ij}^0 represent the conventional elastic stiffness parameters as they can be found in structural mechanics textbooks. It can be noticed that in Eq. (6) damage due to torsion and axial forces are neglected.

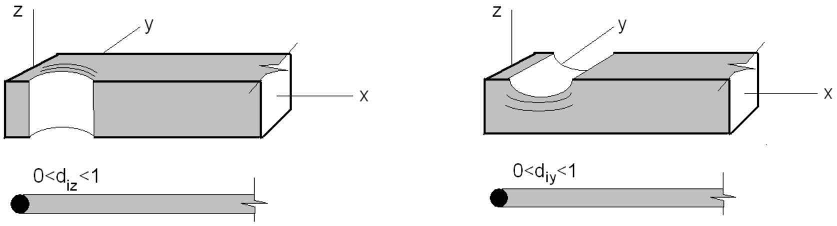

Fig. 3. Characterization of local buckling damage parameters.

Plastic deformation evolution is obtained via the conventional normality law:

$$\begin{aligned} &\dot{\varphi}_{iy}^p = \dot{\lambda}_i \frac{\partial f_i}{\partial m_{iy}}\,;\ \dot{\varphi}_{iz}^p = \dot{\lambda}_i \frac{\partial f_i}{\partial m_{iz}}\,;\ \dot{\delta}^p = \dot{\lambda}_i \frac{\partial f_i}{\partial n} + \dot{\lambda}_j \frac{\partial f_j}{\partial n}\,; \\ &\dot{\varphi}_{jy}^p = \dot{\lambda}_j \frac{\partial f_j}{\partial m_{jy}}\,;\ \dot{\varphi}_{jz}^p = \dot{\lambda}_j \frac{\partial f_j}{\partial m_{jz}}\,;\ \dot{\varphi}_{x}^p = \dot{\lambda}_i \frac{\partial f_i}{\partial m_x} + \dot{\lambda}_j \frac{\partial f_j}{\partial m_x} \end{aligned} \qquad (7)$$

where $\mathrm{f_i} = \mathrm{f_i}(\boldsymbol{\sigma}_e, \mathbf{d}_e) \le 0$ and $\mathrm{f_j} = \mathrm{f_j}(\boldsymbol{\sigma}_e, \mathbf{d}_e) \le 0$ are the yield functions of, respectively, plastic hinges i and j. The plastic multipliers λ_i and λ_j are computed via the usual consistency condition:

$$\begin{cases} \dot{\lambda}_i = 0 & \text{if} \quad \mathrm{f_i} < 0 \quad \text{or} \quad \dot{\mathrm{f}}_\mathrm{i} < 0 \\ \dot{\lambda}_i > 0 & \text{if} \quad \mathrm{f_i} = 0 \quad \text{and} \quad \dot{\mathrm{f}}_\mathrm{i} = 0 \end{cases} \qquad (8)$$

In order to define the damage evolution law, the following set of local buckling driving forces is defined: $(\mathbf{p}_e)^t = (p_{iy}, p_{iz}, p_{jy}, p_{jz})$ where $\dot{p}_{iy} = \left|\dot{\varphi}^p_{iy}\right|$ and so on. It can be seen that p is a matrix of cumulated plastic strains.

The damage evolution law is obtained with the help of two damage functions, $g_i = g_i(\mathbf{p}_e;\mathbf{d}_e) \leq 0$ and $g_j = g_j(\mathbf{p}_e;\mathbf{d}_e) \leq 0$:

$$\begin{aligned} \dot{d}_{iy} &= \dot{\gamma}_i \frac{\partial g_i}{\partial p_{iy}} & \dot{d}_{iz} &= \dot{\gamma}_i \frac{\partial g_i}{\partial p_{iy}} \\ \dot{d}_{jy} &= \dot{\gamma}_j \frac{\partial g_j}{\partial p_{jy}}; & \dot{d}_{jz} &= \dot{\gamma}_j \frac{\partial g_j}{\partial p_{jy}}; \end{aligned} \tag{9}$$

where γ_i and γ_j are damage multipliers that are computed as:

$$\begin{cases} \dot{\gamma}_i = 0 & \text{if} \quad \mathrm{g_i} < 0 \quad \text{or} \quad \dot{\mathrm{g}}_\mathrm{i} < 0 \\ \dot{\gamma}_i > 0 & \text{if} \quad \mathrm{g_i} = 0 \quad \text{and} \quad \dot{\mathrm{g}}_\mathrm{i} = 0 \end{cases} \tag{10}$$

2.3. A finite element for local buckling analysis

In order to carry out the analysis, the time interval [0,T] must be discretized into a set of instants (0, t_1, t_2,...,T). The frame is analyzed only for these times by using a conventional step-by-step method. After discretization, the kinematic equation becomes:

$$\Delta\boldsymbol{\varepsilon}_e = \mathbf{B}(\mathrm{U})_\mathrm{e}\Delta\mathrm{U} \tag{11}$$

where ΔU represents the difference between the values of the variable U in two consecutive time instants ($\Delta U = U(t_i) - U(t_{i-1})$) and so on. The internal variables evolution laws can be written as:

$$\begin{aligned} \Delta\varphi^p_{iy} &= \Delta\lambda_i \frac{\partial f_i}{\partial m_{iy}}; & \Delta\varphi^p_{iz} &= \Delta\lambda_i \frac{\partial f_i}{\partial m_{iz}}; & \Delta\delta^p &= \Delta\lambda_i \frac{\partial f_i}{\partial n} + \Delta\lambda_j \frac{\partial f_j}{\partial n}; \\ \Delta\varphi^p_{jy} &= \Delta\lambda_j \frac{\partial f_j}{\partial m_{jy}}; & \Delta\varphi^p_{jz} &= \Delta\lambda_j \frac{\partial f_j}{\partial m_{jz}}; & \Delta\varphi^p_{x} &= \Delta\lambda_i \frac{\partial f_i}{\partial m_x} + \Delta\lambda_j \frac{\partial f_j}{\partial m_x} \end{aligned} \tag{12}$$

$$\begin{cases} \Delta\lambda_i = 0 & \text{if} \quad \mathrm{f_i} < 0 \\ \Delta\lambda_i > 0 & \text{if} \quad \mathrm{f_i} = 0 \end{cases} \tag{13}$$

$$\Delta d_{iy} = \Delta\gamma_i \frac{\partial g_i}{\partial p_{iy}} \qquad \Delta d_{iz} = \Delta\gamma_i \frac{\partial g_i}{\partial p_{iy}} \tag{14}$$

$$\Delta d_{jy} = \Delta\gamma_j \frac{\partial g_j}{\partial p_{jy}}; \qquad \Delta d_{jz} = \Delta\gamma_j \frac{\partial g_j}{\partial p_{jy}};$$

$$\begin{cases} \Delta\gamma_i = 0 & \text{if} \quad \mathrm{g_i} < 0 \\ \Delta\gamma_i > 0 & \text{if} \quad \mathrm{g_i} = 0 \end{cases} \tag{15}$$

The discretized kinematic equation (11), state law (5) and discretized internal variable evolution laws (12-15) define a relationship between generalized displacements U and generalized stresses $\boldsymbol{\sigma}$ at the end of each step: $\boldsymbol{\sigma}_e = \boldsymbol{\sigma}_e(\mathbf{U})$. Thus, these set of equations define a finite element with local bucking that can be implemented in any nonlinear structural analysis program. Introducing this relationship into the equilibrium equation (4), it is obtained the following expression:

$$\mathbf{L}(\mathbf{U}) = \sum_{e=1}^{m} \mathbf{B}_e^t \boldsymbol{\sigma}(\mathbf{U})_e - \mathbf{F} = 0 \tag{16}$$

Eq. (16) must be solved at each step using any of the conventional algorithms, for instance the Newton-Raphson method.

The relationship $\boldsymbol{\sigma}_e = \boldsymbol{\sigma}_e(\mathbf{U})$ represents a set of nonlinear equations that can also be solved by the Newton-Raphson method. The local buckling model described in the previous section is a multi-criteria plastic-damage model. Algorithms for the numerical computation of stresses in such a case can be found in [15, 16].

3 EXPERIMENTAL ANALYSIS AND NUMERICAL SIMULATION OF LOCAL BUCKLING

The model of local buckling composed by the kinematics equation (11), the state law (5), the equilibrium equation (16), the plastic deformation evolution law (12-13) and the damage evolution law (14-15) was implemented as a new finite element in a commercial structural analysis program [17].

In order to validate the local buckling model, an experimental program was carried out at the Structural Mechanics Laboratory of the Lisandro Alvarado University [18]. The specimens consisted in steel hollow structural elements with circular and rectangular cross-section built in as a cantilever into a heavily reinforced foundation (fig. 4a). The tridimensional structure shown in Fig. 4b was also tested. All the specimens were subjected to bidirectional loading paths. Two servo-controlled 50 Ton-capacity hydraulic actuators applied the desired transverse displacement histories.

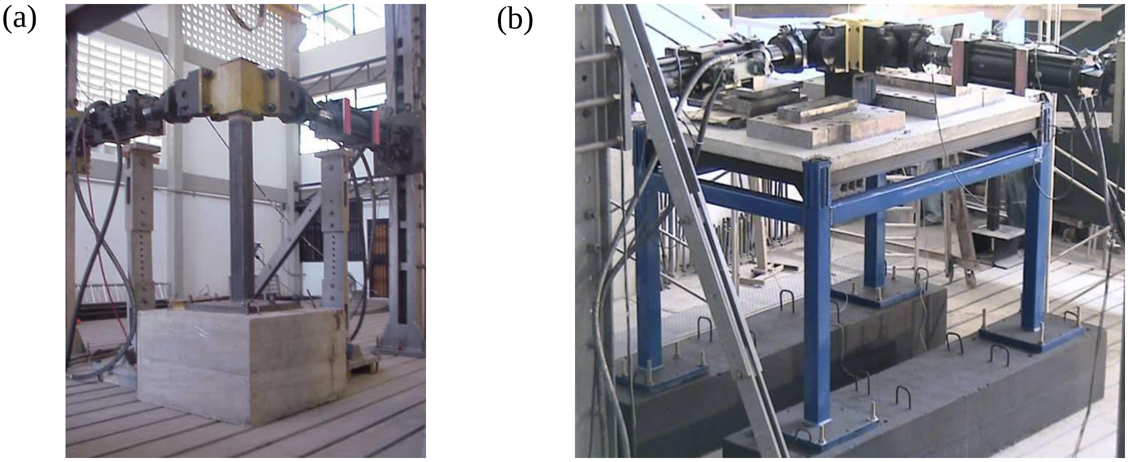

Fig. 4. (a) Setup of the cantilever specimen test. (b) Setup of the tridimensional frame test.

3.1 Elements of circular hollow section

3.1.1 Yield and damage functions

For circular hollow cross-section elements the yield functions for the hinges i and j are [3, 18]:

$$f_i = \left(\frac{N}{N_u}\right)^2 + \left(\frac{M_{iy}}{M_u(1-d_{iy})}\right)^2 + \left(\frac{M_{iz}}{M_u(1-d_{iz})}\right)^2 - 1;$$
$$f_j = \left(\frac{N}{N_u}\right)^2 + \left(\frac{M_{jy}}{M_u(1-d_{jy})}\right)^2 + \left(\frac{M_{jz}}{M_u(1-d_{jz})}\right)^2 - 1 \qquad (17)$$

where N_u is the axial yield load and M_u is the plastic moment of the section. The damage functions are given by [3, 18]:

$$g_i = \left(\frac{p_{iy}}{P_{cr} + \frac{d_{iy}}{c}}\right)^2 + \left(\frac{p_{iz}}{P_{cr} + \frac{d_{iz}}{c}}\right)^2 - 1; \qquad g_j = \left(\frac{p_{jy}}{P_{cr} + \frac{d_{jy}}{c}}\right)^2 + \left(\frac{p_{jz}}{P_{cr} + \frac{d_{jz}}{c}}\right)^2 - 1 \qquad (18)$$

The parameters P_{cr} and c correspond, respectively; to the value of the plastic rotation that initiates the local buckling and the growth rate of the local buckling domain.

3.1.2 Identification test.

In order to obtain the values of the evolution law parameters, a circular element with 127 mm diameter cross-section, 3 mm thickness and a free length of 1.28 m was built as a cantilever as is shown in Fig. 5a and tested applying the displacement-controlled lateral actions shown in Fig. 5b. This test was called CM. Fig. 5d shows the experimental results. The procedure for the identification of parameters M_u, c and P_{cr} in the moment – rotation curve is shown in Fig 5c. It is assumed that local buckling begins with the softening phase.

The experimental results are shown in Fig. 5d and the corresponding numerical simulation in Fig 5e. The geometry was represented by only one finite element that was fixed (nil displacements) at one of the extremes while the other one was subjected to the imposed displacements. The local buckling at the end of the test can be appreciated in Fig. 6a.

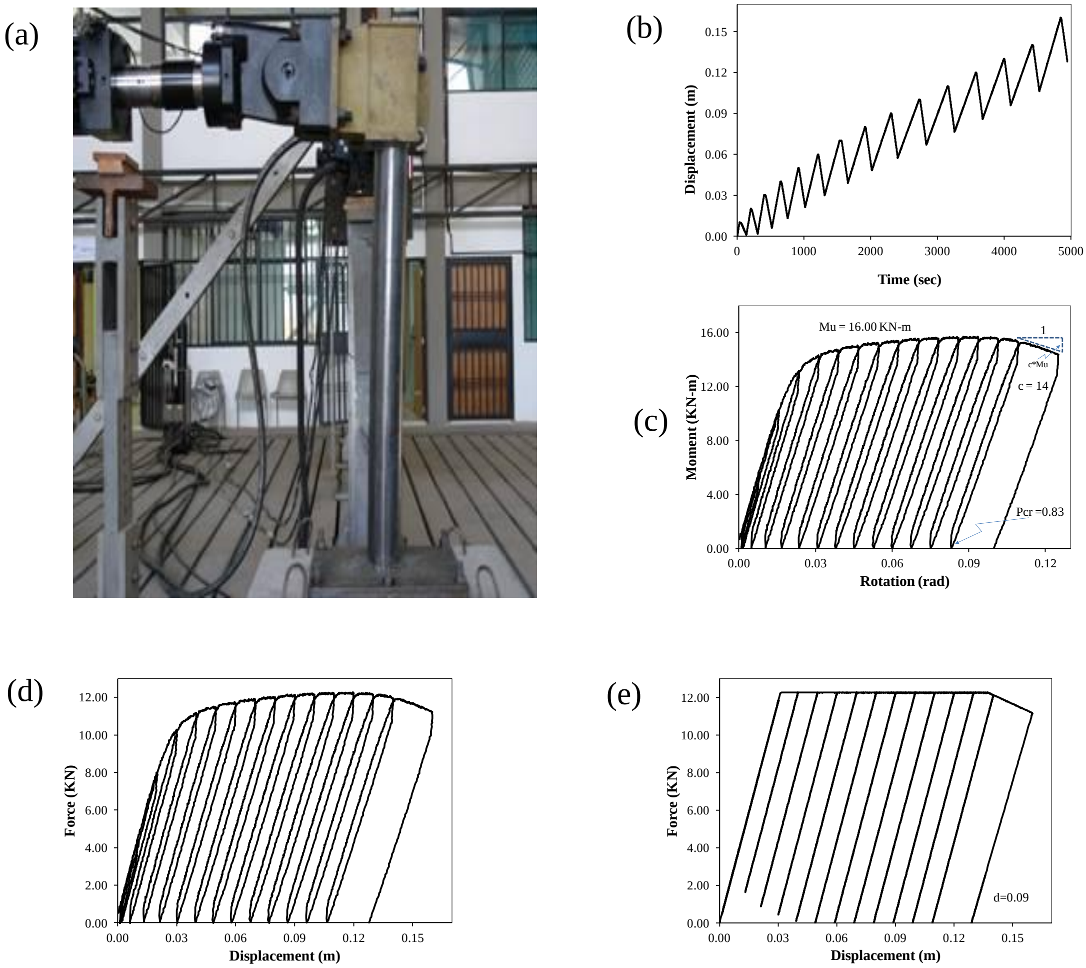

Fig. 5. (a) Element tested (b) Loading path of the test CM. (c) Identification of parameters M_u, c and P_{cr}. (d) Experimental force vs. displacement curve. (e) Numerical simulation.

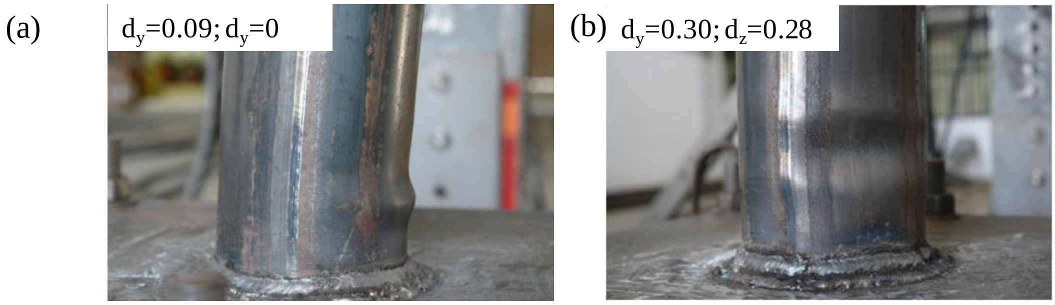

Fig. 6. Local buckling aspect at the end of the test. (a) In the specimen CM (b) In the specimen CT.

3.1.3 Beams subjected to complex loading

In order to calibrate the model, additional tests were performed. Similar specimens were subjected to more complex loading paths. The results of the tests and the corresponding numerical simulations are shown in the present section.

Test and simulation CL

The first one corresponds to a specimen subjected to uniaxial displacements in pairs of linearly increasing amplitude applied alternately in the two orthogonal directions as it is shown in Fig. 7a. Fig. 7b shows the experimental Force z-Force y curve and Fig. 7c the curve obtained with the numerical simulation. Figs. 7d and 7f show the experimental Force-Displacement curves in both orthogonal directions and in Figs. 7e and 7g the corresponding numerical simulations. The values of the damage computed at the end of the test are indicated in the same figures.

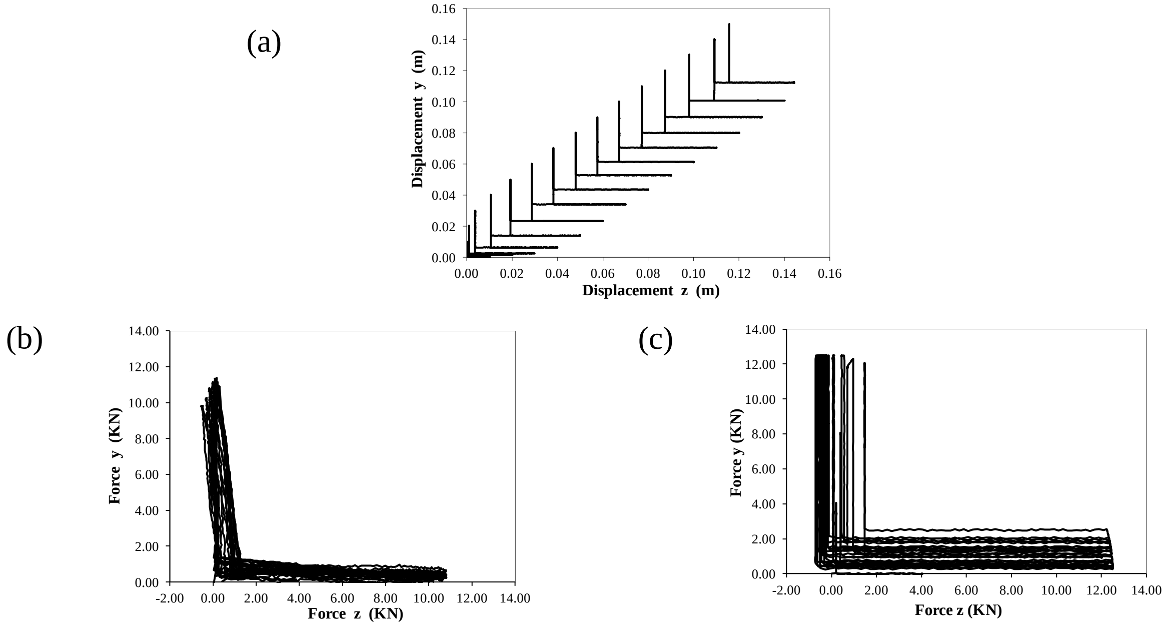

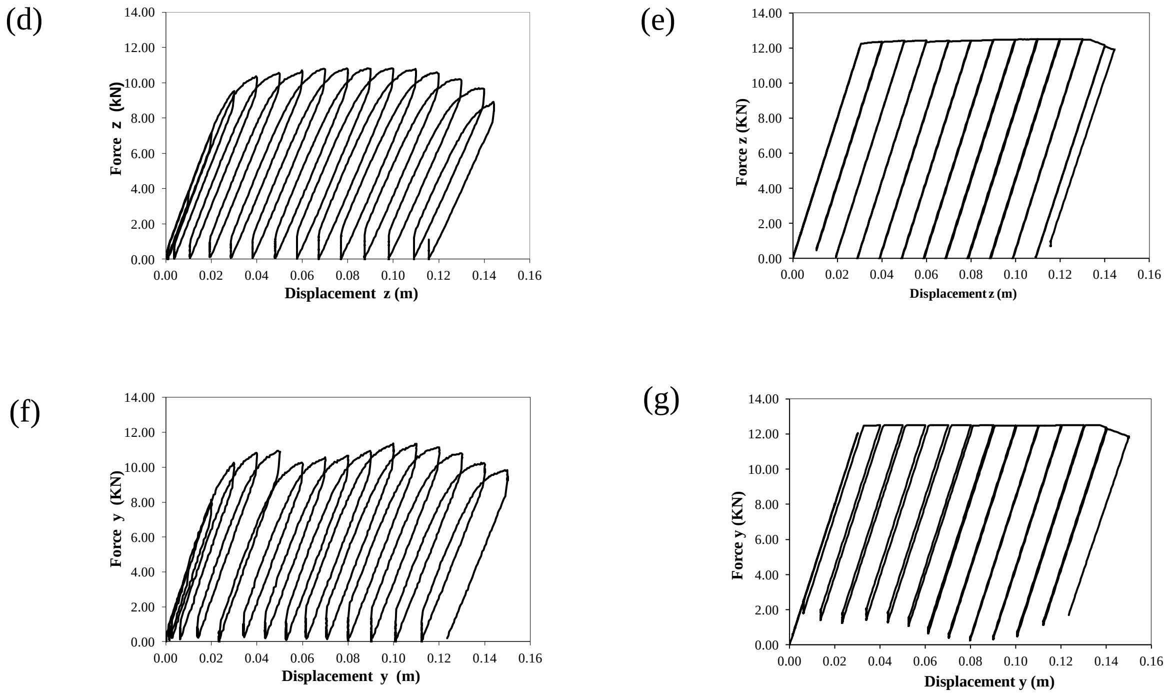

Fig. 7. Test and simulation CL: a) Imposed transverse displacements path. b) Experimental Force z-Force y curve. c) Numerical simulation. d) Experimental Force-Displacements curve in z direction. e) Numerical simulation. f) Experimental Force-Displacements curve in y direction. g) Numerical simulation.

Test and simulation CT

In this test, the specimen was subjected to the triangular-shaped displacements shown in Fig. 8a. To obtain the loading path, displacements of the same magnitude were sequentially applied in the two orthogonal directions and then, the specimen was unloaded simultaneously to zero force. Fig. 8b shows the experimental Force z – Force y curve and Fig. 8c the corresponding numerical simulation. The experimental Force-Displacement curves are indicated in Figs. 8d and 8f and the corresponding numerical simulations in Figs. 8e and 8g. The aspect of the local buckling at the end of the test is presented in Fig. 6b.

Test and simulation CS

In this test, the specimen was subjected to the square-shaped displacements shown in Fig. 9a. To obtain the loading path, displacements of the same magnitude were sequentially applied in the two orthogonal directions and then, the specimen was unloaded to zero force in the same sequence. In Fig. 9b it is shown the experimental Force z – Force y curve and in Fig. 9c the corresponding numerical simulation. The experimental Force-Displacement curves are indicated in Figs. 9d and 9f and the corresponding numerical simulations in Figs. 9e and 9g.

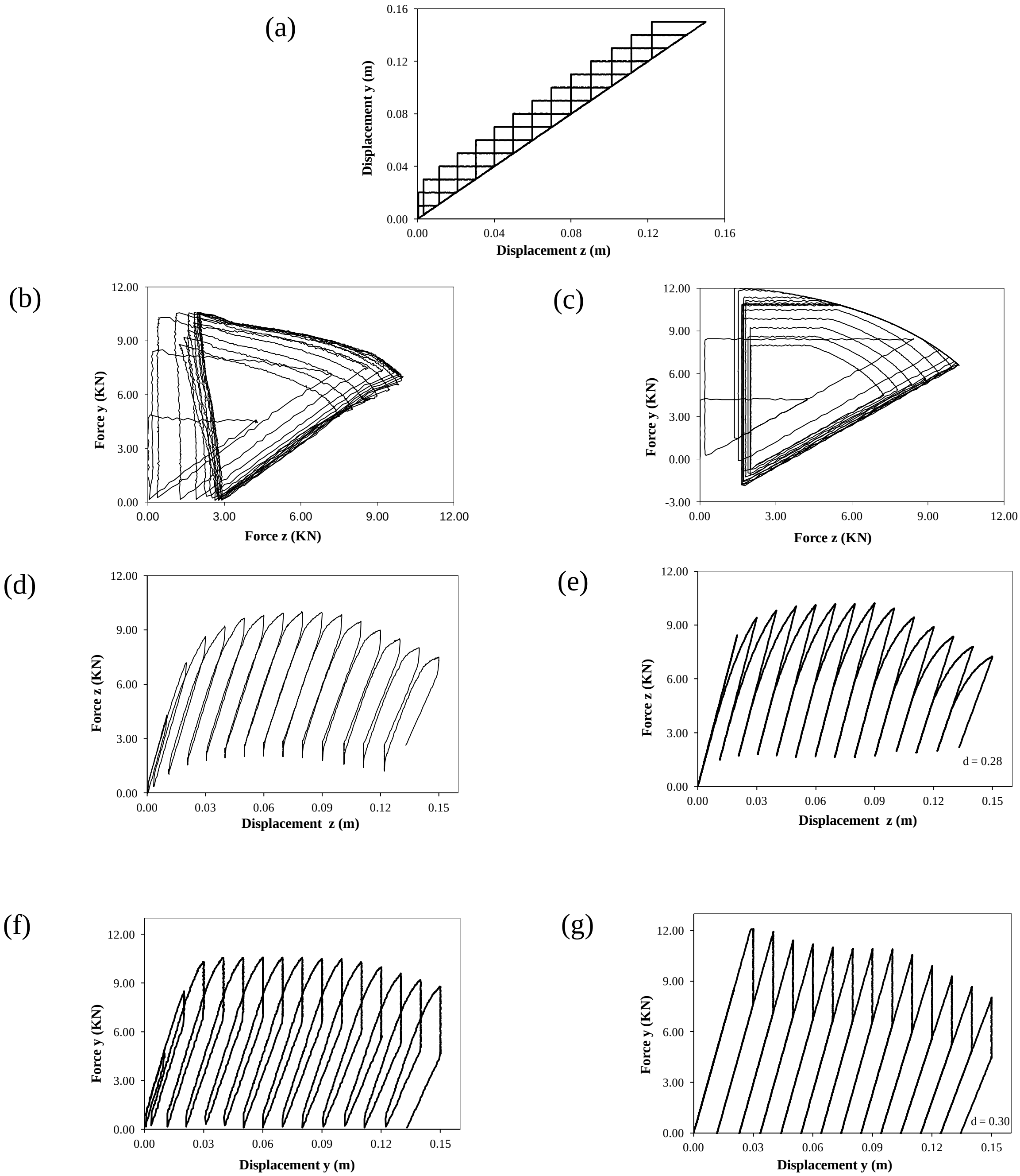

Fig. 8. Test and simulation CT a) Imposed transverse displacements path. b) Experimental Force z-Force y curve. c) Numerical simulation. d) Experimental Force-Displacement curve in z direction.

e) Numerical simulation. f) Experimental Force-Displacement curve in y direction. g) Numerical simulation.

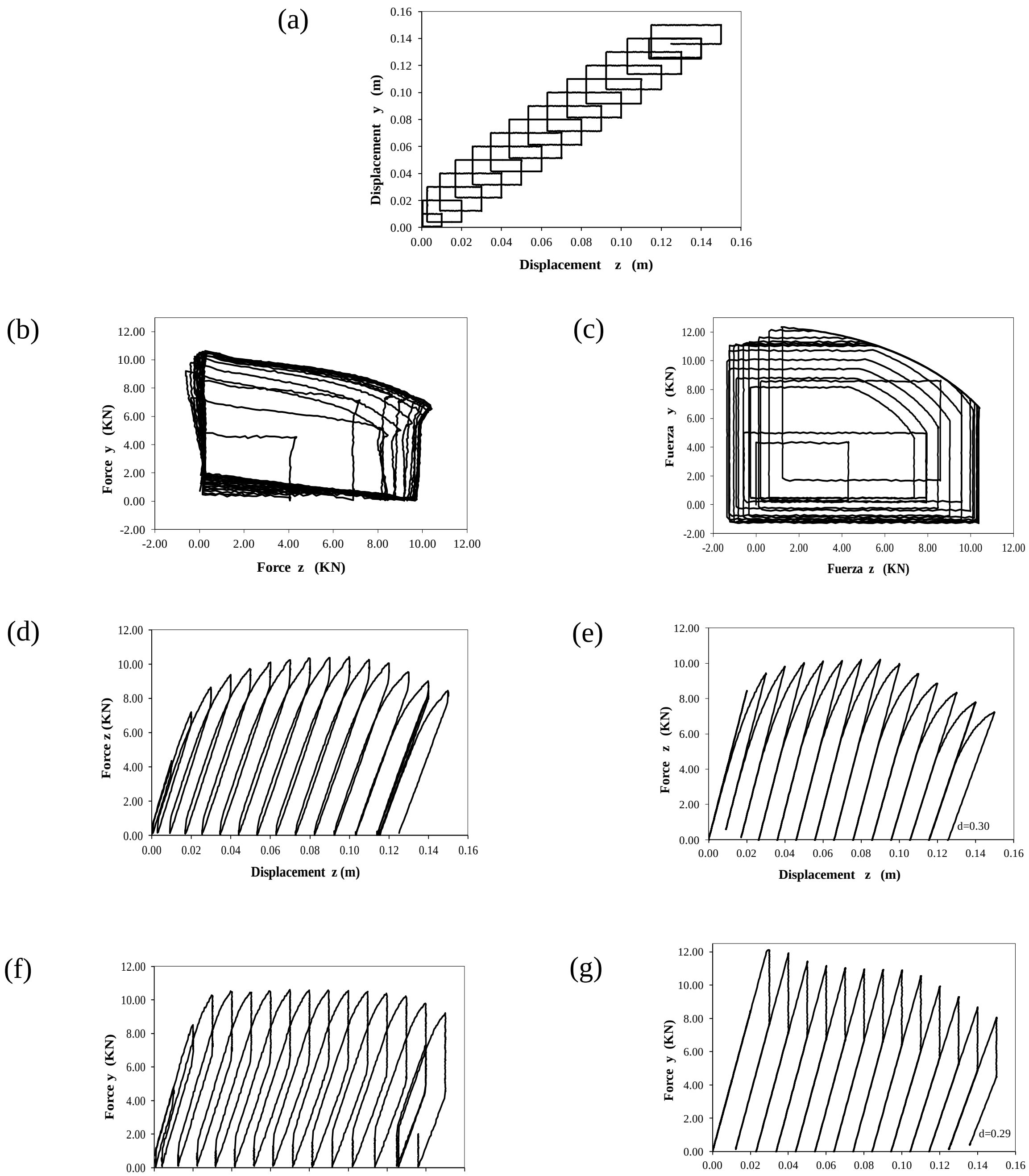

Fig. 9. Test and simulation CS a) Imposed transverse displacements path. b) Experimental Force z-Force y curve. c) Numerical simulation. d) Experimental Force-Displacement curve in z direction. e) Numerical simulation. f) Experimental Force-Displacement curve in y direction. g) Numerical simulation.

3.2 Elements of rectangular hollow section

3.2.1 Yield and damage functions

In the case of elements with rectangular hollow section the yield functions for the hinges i and j are can be written as [3,18]:

$$
\begin{aligned}
f_i &= \left(\frac{N}{N_u}\right)^2 + \left(\frac{M_{iy}}{M_{uy}(1-d_{iy})}\right)^2 + \left(\frac{M_{iz}}{M_{uz}(1-d_{iz})}\right)^2 - 1 \\
f_j &= \left(\frac{N}{N_u}\right)^2 + \left(\frac{M_{jy}}{M_{uy}(1-d_{jy})}\right)^2 + \left(\frac{M_{jz}}{M_{uz}(1-d_{jz})}\right)^2 - 1
\end{aligned}
\qquad (19)
$$

and the damage functions as [3,18]:

$$
g_i = \left(\frac{p_{iy}}{P_{cry} + \dfrac{d_{iy}}{c_y}}\right)^2 + \left(\frac{p_{iz}}{P_{crz} + \dfrac{d_{iz}}{c_z}}\right)^2 - 1; \qquad g_j = \left(\frac{p_{jy}}{P_{cry} + \dfrac{d_{jy}}{c_y}}\right)^2 + \left(\frac{p_{jz}}{P_{crz} + \dfrac{d_{jz}}{c_z}}\right)^2 - 1 \qquad (20)
$$

It can be observed that in this case there are different parameters for both orthogonal directions.

3.2.2 Identification tests

In this case, because of the asymmetry of the cross-section, two monotonic tests were performed, one for each orthogonal direction, in order to identify the parameters M_{uy}, M_{uz}, P_{cry}, P_{cry}, c_y and c_z. The specimens consisted in rectangular elements with 120 x 60 mm cross-section, 2.5 mm thickness and a free length of 1.28 m built as cantilever and tested applying a monotonic displacement as it is shown in Fig. 10a and 10b. These tests were called respectively, RM-Y and RM-Z, where Z is the axis that corresponds to the stronger resistance. Figs. 10c and 10e show the experimental results and the values of the parameters. In Figs. 10d and 10f the corresponding numerical simulations are presented.

In Fig. 11a it is shown the local buckling aspect at the end of the RM-Y test and in Fig. 11b the corresponding to RM-Z.

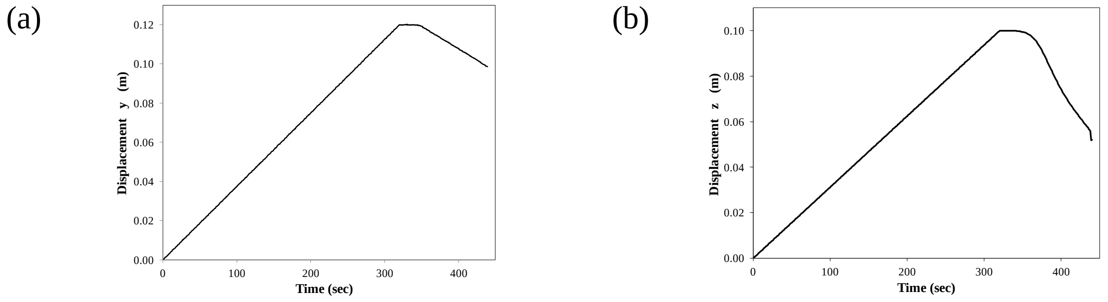

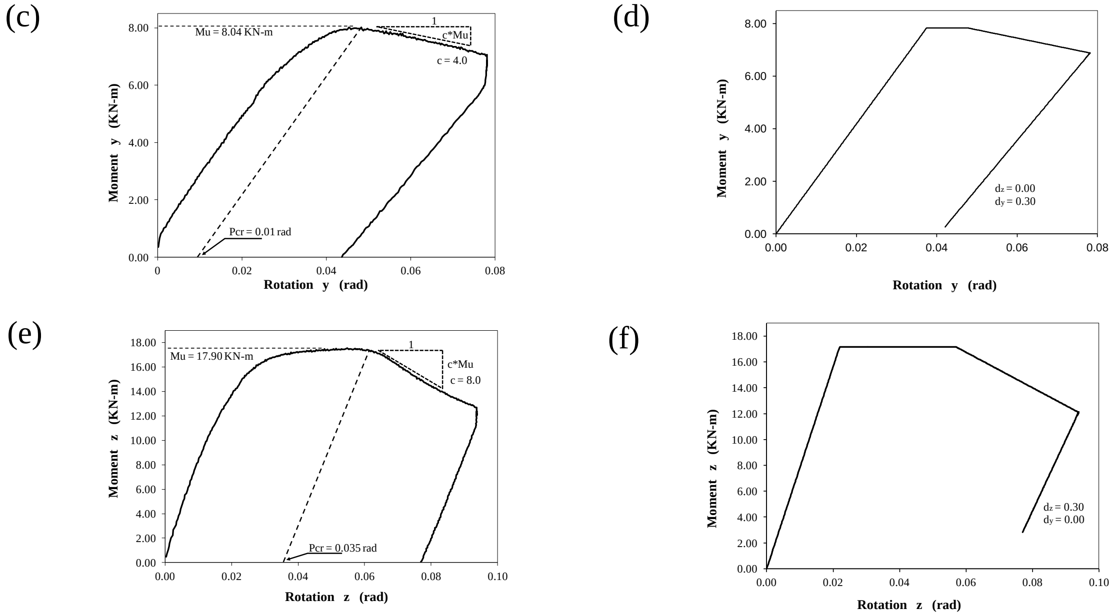

Fig. 10. (a) Displacement history of the test RM-Y. (b) Displacement history of the test RM-Z (c) Experimental Moment vs Rotation curve of the test RM-Y. (d) Numerical simulation of the test RM-Y. (e) Experimental Moment vs Rotation curve of the test RM-Z. (f) Numerical simulation of the test RM-Z.

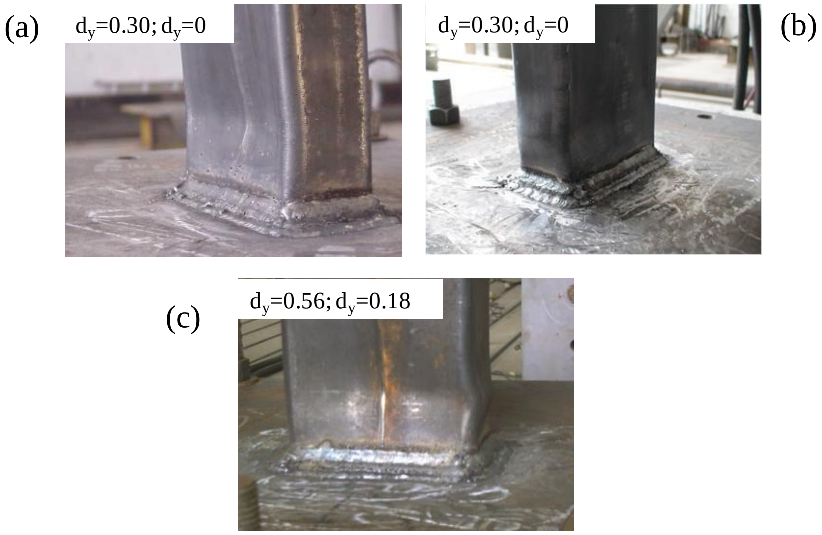

Fig. 11. Local buckling aspect at the end of the test. (a) In the specimen RM-Y; (b) In the specimen RM-Z; (c) In the specimen RT.

3.2.3 Beams subjected to complex loadings

Continuing with the calibration of the model, similar loading paths to those used for the circular specimens were applied in the case of the rectangular ones. The numerical and experimental results are shown below.

Test and simulation RT

In this test it was applied a triangle loading path shown in Fig. 12a. In Fig. 12b the experimental Force z – Force y curve is presented and in Fig. 12c the corresponding numerical simulation. The experimental Force-Displacement curves are indicated in Figs. 12d and 12f and the corresponding numerical simulations in Figs. 12e and 12g. In these figures the values of the damage computed at the end of some elastic unloadings are presented. In Fig. 11c it is shown the local buckling aspect at the end of the test.

(a)

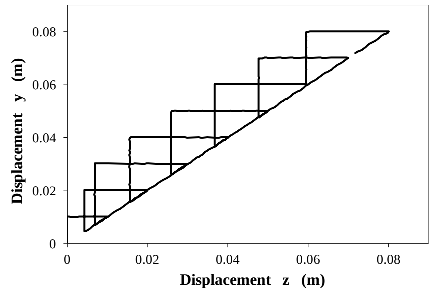

(b)

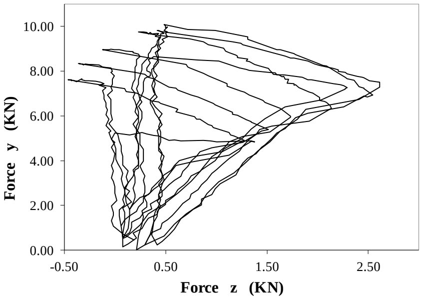

(c)

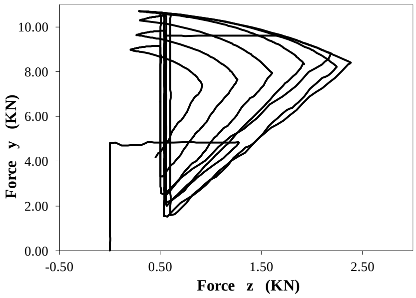

(d)

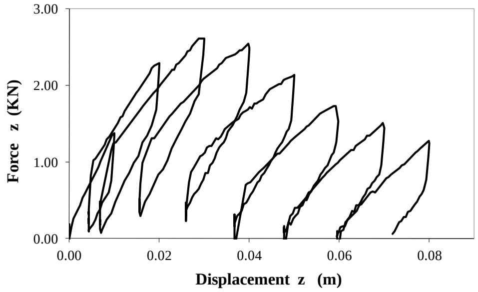

(e)

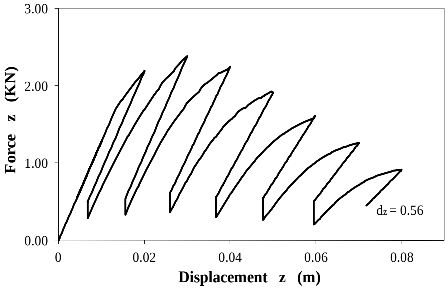

(f)

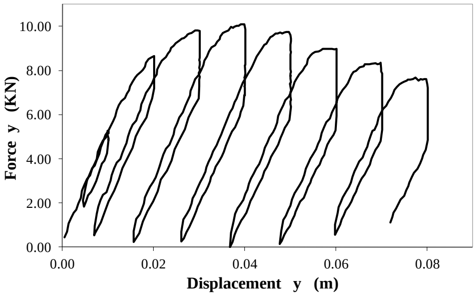

(g)

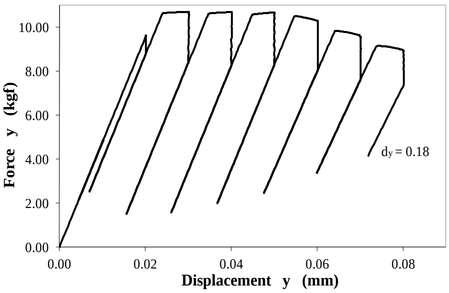

Fig. 12. Test and simulation RT a) Imposed transverse displacements path. b) Experimental Force z-Force y curve. c) Numerical simulation. d) Experimental Force-Displacement curve in z direction. e) Numerical simulation. f) Experimental Force-Displacement curve in y direction. g) Numerical simulation.

Test and simulation RS

In this test, the specimen was subjected to the square-shaped displacements shown in Fig. 13a. In Fig. 13b it is shown the experimental Force z – Force y curve and in Fig. 13c the corresponding numerical simulation. The experimental Force-Displacement curves are indicated in Figs. 13d and 13f and the corresponding numerical simulations in Figs. 13e and 13g.

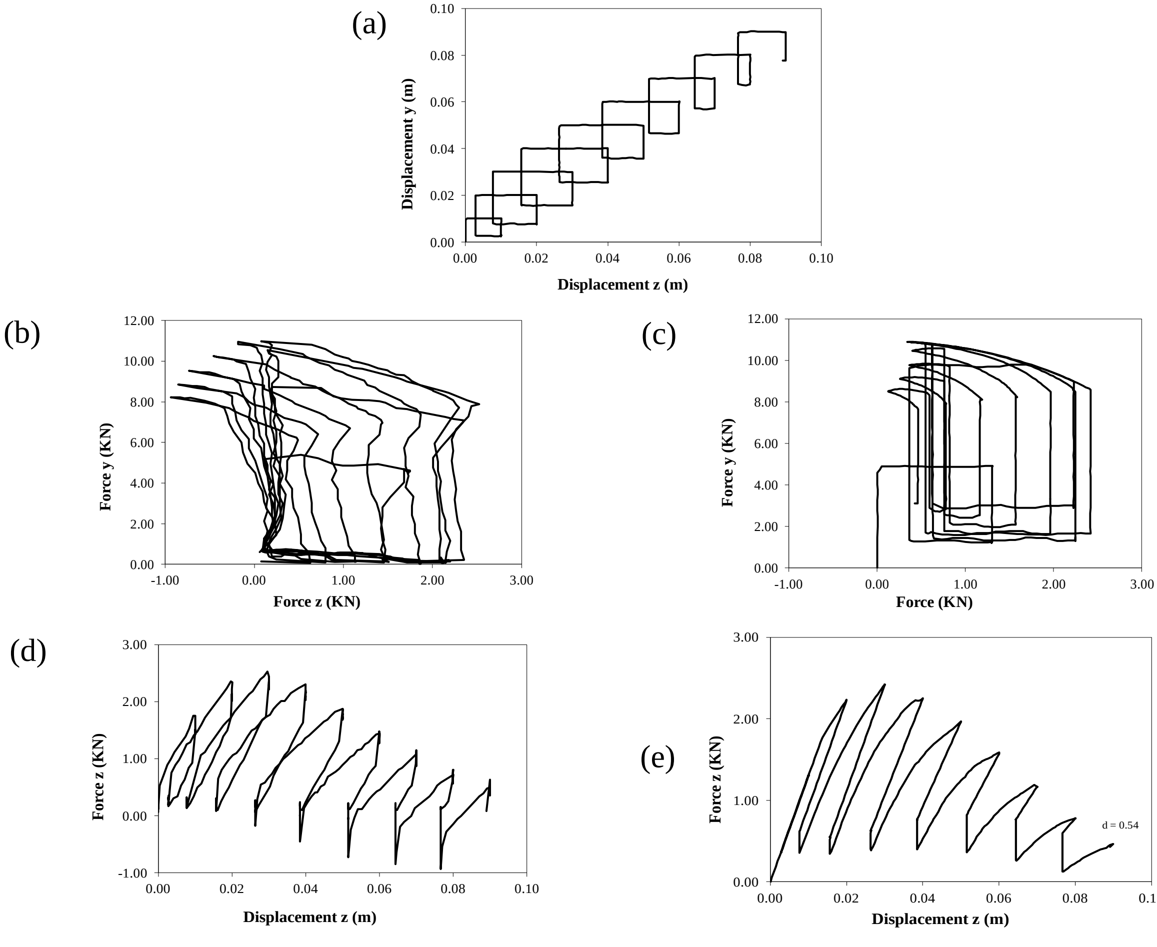

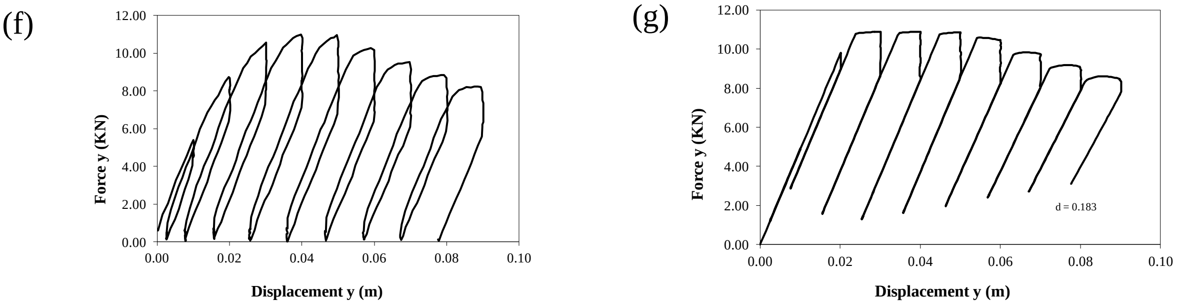

Fig. 13. Test and simulation RS. a) Imposed transverse displacements path. b) Experimental Force z-Force y curve. c) Numerical simulation. d) Experimental Force-Displacement curve in z direction. e) Numerical simulation. f) Experimental Force-Displacement curve in y direction. g) Numerical simulation.

3.3 Tridimensional frame structure

The last example corresponds to the tridimensional frame shown in Fig. 4b. The model parameters used in the numerical simulation are: M_u = 34,33 KN-m, P_{cr} / L = 0,016 m^{-1} and c / L = 3,63 m^{-1}. These values were obtained experimentally.

3.3.1. Experimental results and analysis

The frame was built with steel hollow elements of 120 mm square cross-section and 4 mm thickness. The geometry of the structure is shown in Fig. 14. As it can be observed in this figure, in the upper side of the frame it was built a very rigid structure where the loading path shown in Fig. 15a was applied. The displacements were imposed in the middle of this structure through a steel device specially designed for this purpose (see Fig. 4b). The response was obtained in the displacement application point. The tridimensional frame was fixed to the laboratory's slab through two heavy foundations as it is shown in Fig. 4b.

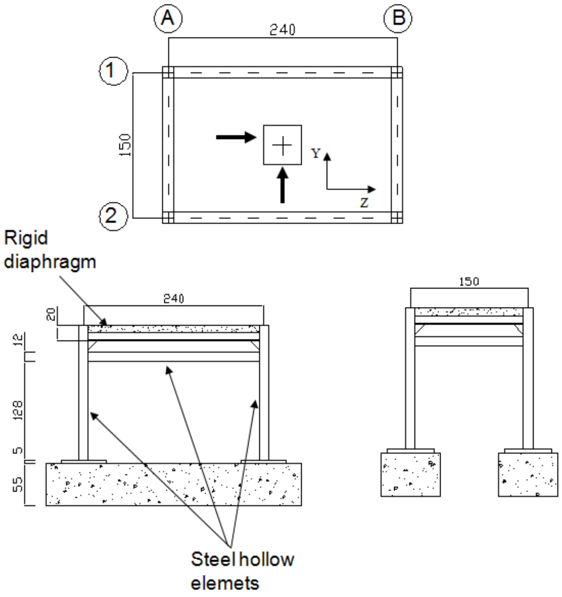

Fig. 14. Geometry of the frame tested

For the numerical simulation of the test, beams and columns of the structure were represented by the finite element described in this paper, one element for each frame member (a total of eight elements). The slab was represented by multiple elastic elements with high stiffness to asses a uniform distribution of the displacements in the tridimensional frame.

In Fig. 15b it is shown the experimental Force Z – Force Y curve and in Fig. 15c the corresponding numerical simulation. The experimental Force-Displacement curves are indicated in Figs. 15d and 15f and the corresponding numerical simulations in Figs. 15e and 15g.

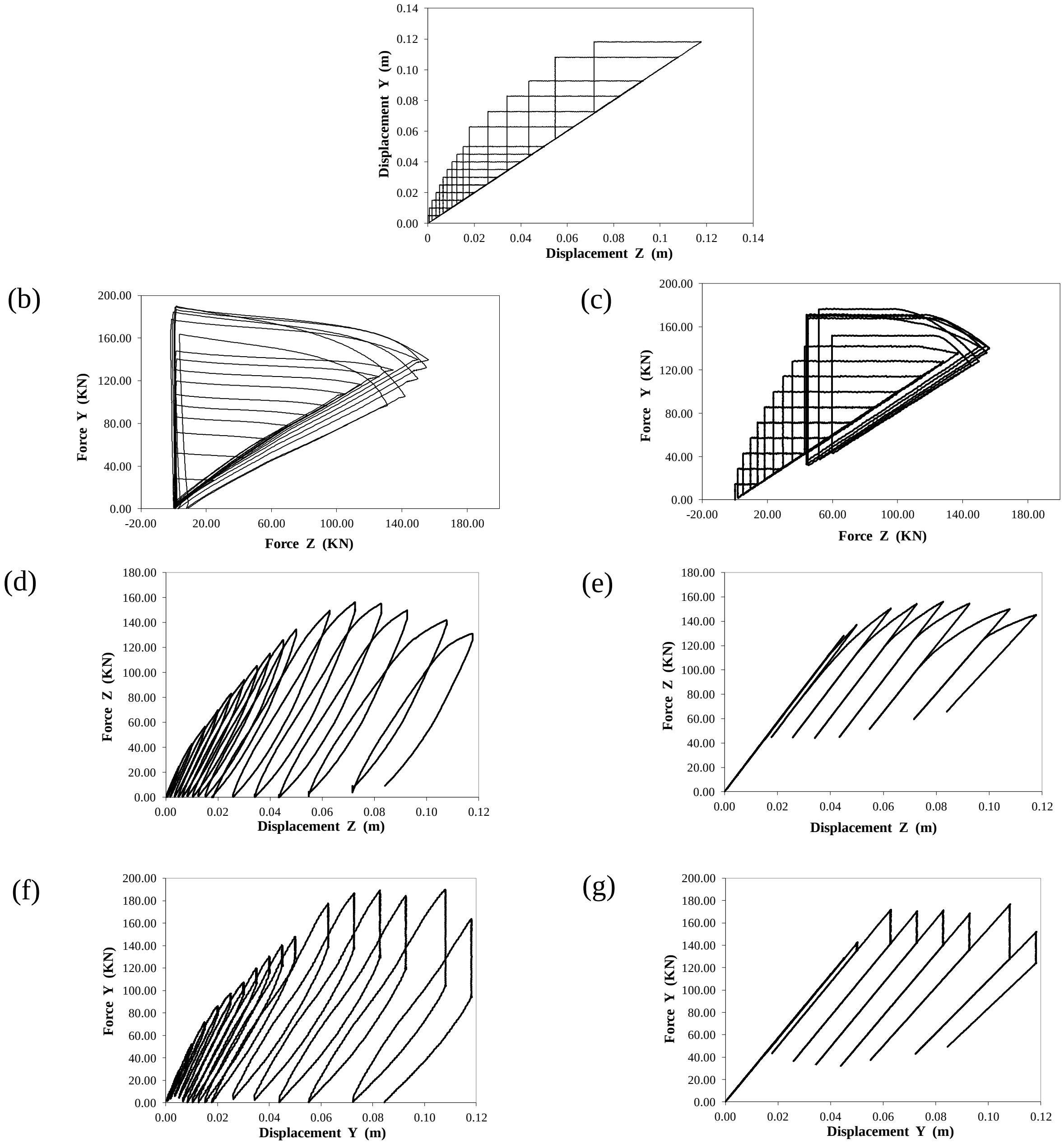

(a)

Fig. 15. Tridimensional frame structure: test and simulation. a) Imposed transverse displacements path. b) Experimental Force Z-Force Y curve. c) Numerical simulation. d) Experimental Force-Displacement curve in Z direction. e) Numerical simulation. f) Experimental Force-Displacement curve in Y direction. g) Numerical simulation.

The damage values and the local buckling aspect in the most damaged column at the end of the test are shown in Fig. 16.

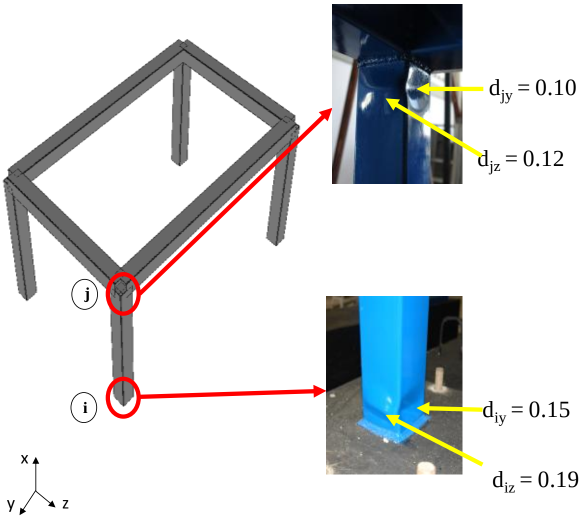

Fig. 16. Damage values and local buckling aspect at the end of the test

4 FINAL REMARKS AND CONCLUSIONS

This paper presents the results of an experimental study that contributes to enrich the limited data base on the post-buckling behavior of hollow steel elements. In particular, it should be noticed the experimental test on the tridimensional structure subjected to bidirectional complex loadings.

It has been shown that lumped damage mechanics is a promising approach for the representation of a complex phenomenon in a simple way. The model gives a good enough description for engineering purposes of the post-buckling behavior of tubular elements and structures. This approach allows the analysis of this behavior of very large structures. This is probably the only way to take into account the interactions of the simultaneous development of local buckling in different parts of a tridimensional structure.

It can be appreciated the good agreement between experimental and numerical results in the examples presented in the paper.

The availability of damage variables that represent in a very simple, quantitative and objective way the local buckling degree is an important advantage taking into account the tendency of the codes to include limits values for damage and residual deformation.

The model can be incorporated in the library of finite elements of any nonlinear structural analysis program.

The model considers a limited numbers of member dependent constants. They have a straightforward physical interpretation and can be experimentally identified in a simple monotonic test.

Taking into account that the tubular structural elements come in a limited number of sizes and shapes it is possible to develop a catalog for them. Alternatively, these parameters could be computed by numerical tests using shell theory. This is a multi-scale procedure that combines shell theory at the local level and lumped damaged mechanics at the global one.

It can be noticed that the model is a modification of a perfect plasticity constitutive equation. The absence of hardening variables gives a schematic representation of the plastic phase of the behavior. As a result the structural behavior is better represented at the final part of the force-displacement curves than at the beginning. The model can be improved by including plastic hardening terms but this increases its mathematical complexity.

The accuracy of the model diminishes if there are important variations of the axial loads. The cyclic loading case is not well represented by this simple model because the presence of the counter-buckling effect that consists in the "ironing" of the buckling "wrinkles" when moments change sign. This is still an open subject although some clues can be found in [14].

Acknowledgment

The results presented in this paper were obtained in the course of an investigation sponsored by FONACIT and CDCHT-UCLA.

References

[1] E. Watanabe, K. Sugiura and W. Oyawa, Effects of multidirectional displacement paths on the cyclic behavior of rectangular hollow steel columns, *J Struct Mech and Earthquake Eng,* 647 (1–51) (2000), pp. 69–85.

[2] Y. Goto,. K. Jiang, M. Obata, Stability and ductility of thin-walled circular steel columns under cyclic bidirectional loading, *J Struct Eng,* 132 (10) (2006), pp. 1621-1631.

[3] N. Guerrero, M.E. Marante, R. Picón, J. Flórez-López, Model of local buckling in steel hollow structural elements subjected to biaxial bending, *J Construct Steel Res*; 63 (6) (2007), pp.779-790.

[4] L.A. Fahnestock, J.M. Ricles, R. Sause, Experimental evaluation of a large-scale buckling-restrained braced frame, *J Struct Eng*; 33 (9) (2007), pp.1205-1214.

[5] B. Qu, M. Bruneau, C.H. Lin, K.C. Tsai, Testing of full-scale two-story steel plate shear wall with reduced beam section connections and composite floors, *J Struct Eng*, 134 (3) (2008), pp. 364-373.

[6] C.D. Annan, M.A. Youssef, M.H. El Naggar, Experimental evaluation of the seismic performance of modular steel-braced frames, *Eng Struct*; 31 (2009), pp.1435-1446.

[7] J.V. Wood and J.L. Dawe, Full-scale test behavior of cold-formed steel roof trusses. *J Struct Eng*, 132 (4) (2006), pp. 616-623.

[8Nakashima, T. Matsumiya, K. Suita, F. Zhou, Full-scale test of composite frame under large cyclic loading, *J Struct Eng,* 133 (2) (2007), pp. 297-304.

Salem, M.E. Aghoury, F.F. El Dib, M.T. Hanna, Strength of biaxially loaded slender I-section beam–columns, *Can J Civ Eng,*; 734 (2007), pp. 219-227.

Nowzartash and M. Mohareb, Plastic interaction relations for elliptical hollow sections, *Thin-Walled Struct*; 47 (2009), pp. 681-691.

Bebiano, N. Silvestre, D. Camotim, GBT formulation to analyze the buckling behavior of thin-walled members subjected to non-uniform bending, *Int J Struct Stab Dyn,* 7 (1) (2007), pp. 23-54.

Degee, N. Boissonnade, B. Rossi, Local and interactive post-buckling of RHS thin-walled members - comparing a new special beam finite element with shell FE models, *Int J Struct Stab Dyn,* 7 (2) (2007), pp. 213-241.

Inglessis, S. Medina, A. López, R. Febres, J. Flórez-López, Modeling of local buckling in tubular steel frames by using plastic hinges with damage, *Steel Comp Struct,* 2 (1) (2002), pp. 21-34.

Febres, P. Inglessis, J. Flórez López, Modeling of local buckling in tubular steel frames subjected to cyclic loading, *Comput Struct,* 81 (2003), pp. 2237-2247.

[15] J. Simo, A. Kennedy, S. Govindjee, Non-smooth multisurface plasticity and viscoelasticity. Loading/unloading conditions and numerical algorithms, *Int J Num Meth Eng*, 26 (1988), pp. 2161-2185.

[16] G. Maier, L. De Donato, L. Corradi, Inelastic analysis of reinforced concrete frames by quadratic programming, *Symp on inelasticity and nonlinearities in Struct Conc*, University of Waterloo, Canada 1973.

[17] ABAQUS User's manual Hibbitt, Karlsson & Sorensen, Inc. Version 6.5-4.

[18] N. Guerrero, Análisis de vigas de acero estructural de pared delgada sometidas a flexión biaxial (in Spanish), *Doctoral Thesis,* University of Los Andes, Mérida, Venezuela, 2007.